MATERIALS SCIENCE

Enhancing the phase stability of ceramics under radiation via multilayer engineering

Hongliang Zhang[1]*[†], Jianqi Xi[1]*[†], Ranran Su[1][†], Xuanxin Hu[1], Jun Young Kim[1], Shuguang Wei[1], Chenyu Zhang[1], Liqun Shi[2], Izabela Szlufarska[1]*

In metallic systems, increasing the density of interfaces has been shown to be a promising strategy for annealing defects introduced during irradiation. The role of interfaces during irradiation of ceramics is more unclear because of the complex defect energy landscape that exists in these materials. Here, we report the effects of interfaces on radiation-induced phase transformation and chemical composition changes in SiC-Ti_3SiC_2-TiC_x multilayer materials based on combined transmission electron microscopy (TEM) analysis and first-principles calculations. We found that the undesirable phase transformation of Ti_3SiC_2 is substantially enhanced near the SiC/Ti_3SiC_2 interface, and it is suppressed near the Ti_3SiC_2/TiC interface. The results have been explained by ab initio calculations of trends in defect segregation to the above interfaces. Our finding suggests that the phase stability of Ti_3SiC_2 under irradiation can be improved by adding TiC_x, and it demonstrates that, in ceramics, interfaces are not necessarily beneficial to radiation resistance.

INTRODUCTION

Engineering materials with a high density of interfaces have been shown to be a promising strategy for improving the properties of materials, such as mechanical strength (hardness, Young's modulus) (*1*), fracture toughness (*2*), wear resistance (*3*, *4*), and oxidation resistance (*5*, *6*). Interfaces can also act as sinks for nonequilibrium defects (*7*, *8*). Under irradiation, numerous Frenkel pairs are generated by the bombardment of incident neutrons or ions. These defects can either recombine with each other or migrate to defect sinks, such as interfaces (*9*–*11*). If interfaces can efficiently absorb defects, they can be used to design new radiation-resistant materials.

The effects of interfaces have been studied in the context of nanocrystalline materials, where the grain size is decreased to the nanometer regime. In nanocrystalline metals, a high density of grain boundaries (GBs) has been shown to lead to a significant reduction in the number of radiation-induced voids (*12*–*14*). Radiation effects have also been studied in nanocrystalline ceramics, but the results are more complicated. For example, some studies of nanocrystalline SiC with a high density of GBs have shown a substantially enhanced recombination of interstitials and vacancies, leading to self-healing of radiation-induced defects (*15*–*17*). Other studies on nanocrystalline SiC showed the opposite results (*18*, *19*). The seemingly contradicting results in SiC have been explained in terms of the effects of other microstructural features (e.g., stacking faults) on the energy barriers to defect recombination (*9*, *10*, *18*, *19*).

The effect of interfaces on radiation damage recovery/radiation resistance has also been studied in multilayer systems. For example, it has been shown that interfaces in Cu-Nb multilayers are nearly completely void-free when the layer thickness was reduced to less than 30 nm (*14*). The Cu-V multilayers were found to have enhanced radiation tolerance, i.e., they showed a reduction of swelling and suppression of radiation hardening as compared to monolithic Cu or V

(*20*). Studies of radiation effects in multilayer systems have been focused on metallic systems, and similar studies of ceramic multilayers have been limited.

Here, we investigate the radiation resistance of multilayers made of MAX phases (M = early transition metal, A = group A element in the periodic table, and X = C or N), SiC, and TiC. A previous study on a similar material system considered Ti_3SiC_2 with TiC precipitates, and it was found that there was a defect-free zone at the interface between Ti_3SiC_2 and TiC (*21*). However, the authors focused on the characterization of the radiation-induced dislocation loops and lines rather than the interactions between interfaces and radiation-induced point defects. Here, we study a SiC-Ti_3SiC_2-TiC multilayer system and focus on the effects of interfaces on radiation-induced damage and phase transformation and on the mechanisms of defect annihilation by the interfaces.

SiC, TiC, Ti_3SiC_2 are all promising materials for the application as structural and coating materials in nuclear reactors. The MAX phases have superior resistance to radiation-induced amorphization compared to conventional ceramics (*22*, *23*). Ti_3SiC_2 is one of the MAX phases that have been confirmed to have nearly the best radiation tolerance to radiation-induced amorphization and cracks among MAX phase materials (*24*). However, unlike traditional binary carbides (e.g., SiC and TiC), Ti_3SiC_2 is relatively soft and has a low wear resistance (*25*). To counteract this, El-Raghy and Barsoum (*26*) improved the surface hardness of Ti_3SiC_2 by adding TiC and SiC precipitates. There is also evidence indicating that a system containing SiC/Ti_3SiC_2 and Ti_3SiC_2/TiC interfaces will have improved surface hardness and oxidation resistance. This has been shown on the example of Ti_3SiC_2 containing SiC and TiC precipitates (*5*, *27*, *28*). For these reasons, Ti_3SiC_2 with SiC and/or TiC materials are considered as potential coatings, oxygen gettering materials, inert matrices for advanced high-temperature reactor fuels, and structural materials (*29*). Moreover, the synthesis of Ti_3SiC_2 is complicated and usually accompanied by some second phases of TiC and SiC. Therefore, the SiC/Ti_3SiC_2 and TiC/Ti_3SiC_2 interfaces are very common in Ti_3SiC_2.

Although Ti_3SiC_2 does not amorphize up to a very high radiation dose, it has been shown to undergo radiation-induced phase transformation, which can lead to deterioration of mechanical properties

[1]Department of Materials Science and Engineering, University of Wisconsin-Madison, Madison, WI 53706, USA. [2]Institute of Modern Physics, Fudan University, Shanghai 200433, China.
*Corresponding author. Email: hzhang694@wisc.edu (H.Z.); jxi4@wisc.edu (J.X.); szlufarska@wisc.edu (I.S.)
†These authors contributed equally to this work.

and microstructure stability. Phase transformation in these materials has been argued to be driven by chemical compositional changes (30) and/or by the formation and accumulation of defects (31, 32). As TiC is naturally substoichiometric and C poor (i.e., has a large number of C vacancies) (33), the existence of TiC can affect the defect behaviors and chemical composition in Ti_3SiC_2, especially in the near-interface regions. It is therefore an interesting question whether a large density of interfaces (as present in the SiC-Ti_3SiC_2-TiC multilayer system) can suppress the undesirable phase transformation. Here, the role of interfaces in radiation resistance of the SiC-Ti_3SiC_2-TiC multilayer system is investigated using a combination of experimental characterizations and first-principles calculations.

RESULTS

The bright-field transmission electron microscope (TEM) was used to analyze the unirradiated sample as well as the samples irradiated at 7.5×10^{16} ions·cm^{-2} [low dose, ~5 displacements per atom (dpa)], 1.5×10^{17} ions·cm^{-2} (medium dose, ~10 dpa), and 3.0×10^{17} ions·cm^{-2} (high dose, ~20 dpa) (see fig. S1). In the low-dose irradiated sample, the damage peak region contains a high density of black-spot defects, whereas for the medium- and high-dose irradiations, the peak regions become amorphous after irradiation. The amorphous regions of the medium- and high-dose irradiated samples include parts of the SiC-Ti_3SiC_2 interface regions, making it difficult to analyze the changes of the microstructure. Therefore, we chose the low-dose irradiated sample for further analysis of the SiC/Ti_3SiC_2 and TiC/Ti_3SiC_2 interface regions. On the basis of the SRIM (Stopping and Range of Ions in Matter) simulations, the dose in the $SiC/Ti_3SiC_2/TiC$ interface region of the low-dose irradiated sample is about 5 dpa. Figure 1 shows the high-resolution TEM image and the fast Fourier transform (FFT) patterns of the unirradiated and low-dose irradiated samples observed from the $[11\bar{2}0]$ direction of the SiC substrate. There is a single-crystal Ti_3SiC_2 film with a thickness of about 30 nm between the SiC substrate and the TiC film. After irradiation, part of the SiC substrate in the near-interface region became substantially disordered, whereas the deeper region of the SiC substrate retained its crystalline structure. According to the results from SRIM calculations, the deeper region in the SiC substrate should have a higher dpa damage. This finding indicates that the damage level in the SiC/

Ti_3SiC_2 interface region is higher than that in the deeper region, despite the fact that the interface region has experienced a lower radiation dose.

The Ti_3SiC_2 layer near the SiC/Ti_3SiC_2 interface has undergone a phase transformation from a hexagonal close-packed (hcp) Ti_3SiC_2 phase to a new phase after irradiation (see Fig. 1B). On the basis of a combination of indexed FFT patterns and high-resolution TEM from $(11\bar{2}0)$ and $(10\bar{1}0)$ directions of SiC substrate, we have confirmed that the new phase is a face-centered cubic (fcc) phase. We also analyzed the $SiC/Ti_3SiC_2/TiC$ interface regions of the medium-dose (10 dpa) and high-dose (20 dpa) irradiated samples. As shown in Fig. 2A, the SiC/Ti_3SiC_2 interface region of the unirradiated sample showed a very uniform structure of hcp phase Ti_3SiC_2. After the low-dose irradiation, part of the Ti_3SiC_2 film (with a thickness of ~11 nm, about 37%) transformed from the hcp to fcc structure, and some SiC in the near-interface region became amorphous (Fig. 2B). As the dose increased to 10 dpa (medium dose), a larger part of the Ti_3SiC_2 film (with a thickness of ~19 nm, about 63%) transformed from hcp to fcc, and SiC became almost entirely amorphous (Fig. 2C). When the irradiation dose became even larger (Fig. 2D), nearly all of the Ti_3SiC_2 film (with a thickness of more than 25 nm, about 83%) transformed from the hcp to fcc structure, with only ~5 nm of Ti_3SiC_2 close to the TiC layer remaining in the hcp structure. Under this irradiation dose, SiC became entirely amorphous. These results indicate that interfaces play an important role in the radiation-induced phase transformation of Ti_3SiC_2 and that the SiC/Ti_3SiC_2 interface provides a lower resistance to such transformation than the Ti_3SiC_2/TiC interface.

According to previously reported studies (34, 35), the fcc Ti_3SiC_2 forms in the hcp Ti_3SiC_2 most likely as a result of radiation damage.
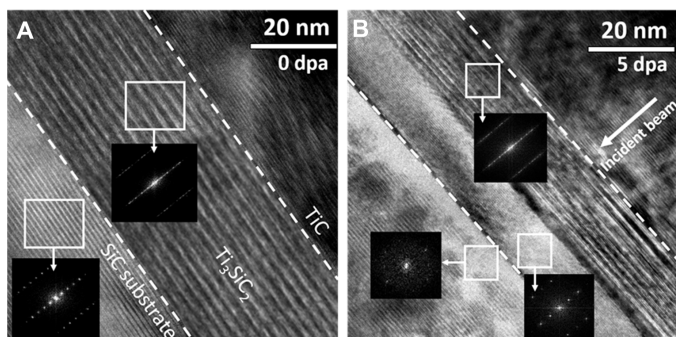

Fig. 1. High-resolution TEM images of the SiC-Ti₃SiC₂-TiC samples viewed from the (11̄20) direction of SiC substrate. (**A**) Before irradiation and (**B**) after RT irradiation at a low dose (7.5×10^{16} ions·cm^{-2}, 5 dpa). The arrow in (B) shows the direction of the incident ion beam. The FFT patterns in (A) show hcp structures of Ti_3SiC_2 and SiC. The FFTs in (B) show fcc structure (bottom right), nearly amorphous structure (bottom left), and hcp structure (top).
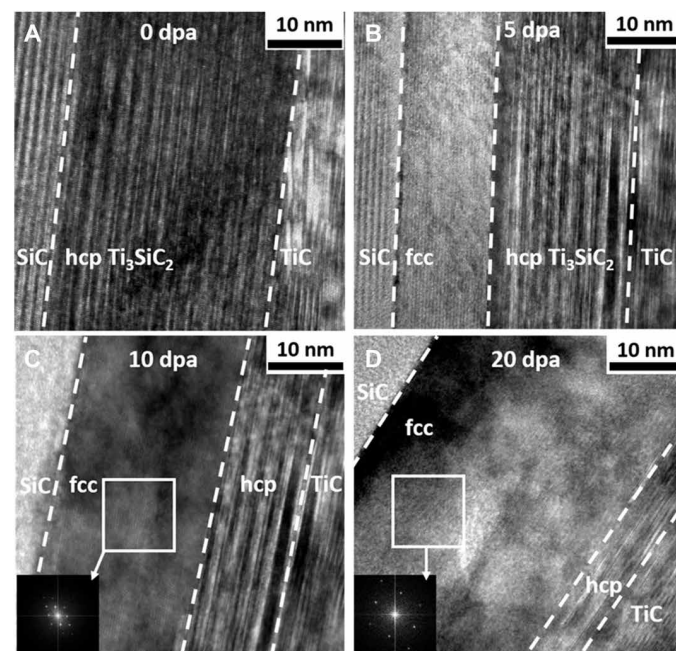

Fig. 2. High-resolution TEM images of the SiC/Ti3SiC2/TiC interface region from the (11̄20) direction. (**A**) Unirradiated and (**B** to **D**) carbon irradiated SiC/Ti_3SiC_2 multilayer sample. The radiation fluences are (B) 7.5×10^{16} ions·cm^{-2} (low dose), (C) 1.5×10^{17} ions·cm^{-2} (medium dose), and (D) 3.0×10^{17} ions·cm^{-2} (high dose). Dashed lines are added to mark interfaces.

Two possible mechanisms for this radiation-induced phase transformation have been proposed: (i) The formation of fcc phase is due to the decomposition of Ti_3SiC_2 into an fcc-structured binary TiC_x, in which the process is accompanied by the out-diffusion of Si atoms (chemical compositional changes) (36, 37), or (ii) the fcc phase is caused by the formation and accumulation of the antisite defects of Ti and Si, followed by a reconstruction of the unit cell (35). According to these two mechanisms, the fcc phase could be either TiC_x or $(Ti_3Si)C_2$, respectively. To determine the nature of the fcc phase, aberration-corrected scanning transmission electron microscopy–energy-dispersive x-ray spectroscopy (STEM-EDS) was used to check the elemental composition in this region. On the basis of multiple measurements taken in different regions of the interface between the fcc and hcp Ti_3SiC_2, we calculated the average Ti, Si, and C concentrations as a function of the distance from the fcc-hcp interface. The results are plotted in Fig. 3C. The results show that the fcc and hcp regions have comparable chemical compositions, indicating that the fcc phase is still a nearly stochiometric Ti_3SiC_2. More specifically, the Si content in the fcc structure region [~18 atomic % (at %)] is slightly higher than that in the hcp structure region (~16 at %), and C content is lower in the fcc structure (~30% in fcc versus ~33% in hcp). Ti content is almost the same in the fcc structure and the hcp region (~50 at %). On the basis of the atomic percentages shown in Fig. 3C, the compositional analysis strongly suggests that the fcc phase that forms in our experiments in Ti_3SiC_2 is not driven by out-diffusion of Si and transformation to TiC_x, as proposed for bulk Ti_3SiC_2 in (37). The second mechanism of phase transformation proposed in the literature for bulk Ti_3SiC_2 (35), which is the formation and accumulation of Ti and Si antisites, cannot be proven by the chemical analysis shown in Fig. 3C, but at least it is not ruled out based on this analysis.

Next, we ask why the radiation-induced phase transformation in Ti_3SiC_2 occurs more readily near the SiC interface than near the TiC interface. In general, there could be several possible reasons for a radiation-induced phase transformation: the strain caused by lattice mismatch between layers, radiation-induced strain, and radiation-induced changes in chemical composition. The lattice mismatch is unlikely to drive the transformation. For unirradiated materials, the lattice parameters (LPs) of 4H-SiC (space group $P6_3mc$) are a-LP = 3.074 Å and c-LP = 10.128 Å, the LPs of Ti_3SiC_2 (space group $P6_3/mmc$) are a-LP = 3.073 Å, c-LP = 17.756 Å, and the LP of TiC (space group $Fm3m$) is a-LP = 3.066 Å. The a-LPs are comparable to each other among the three systems, and even if the difference in a-LPs played a role, this difference is smaller for the SiC/Ti_3SiC_2 pair than for the TiC/Ti_3SiC_2 pair of materials. SiC and Ti_3SiC_2 have c axes aligned because of the way that the films grew. The radiation-induced strain is also unlikely to drive this phase transformation (a detailed explanation is shown in the Supplementary Materials).

We hypothesize that phase transformation near the Ti_3SiC_2 interfaces with SiC and TiC is strongly affected by the radiation-induced changes in chemical compositions near these interfaces. To analyze these changes, we have carried out aberration-corrected STEM-EDS measurements on unirradiated and irradiated samples in regions containing the SiC/Ti_3SiC_2 interface and the TiC/Ti_3SiC_2 interface as well as in bulk SiC and TiC regions (far away from the interface). Figure 4 shows an example of the STEM images and EDS spectra of the region near the SiC/Ti_3SiC_2 interface before and after low-dose irradiation at room temperature (RT). To ensure that the results are reproducible, for each sample, five different locations along the interface were scanned, and the reported results were averaged over the five measurements. The EDS spectra show that, in the unirradiated sample, the interface seems to have a width of about 2 nm, where there seems to be either some Ti in SiC or depleted C. After irradiation, the RT low-dose irradiated sample has a higher Si atomic % near the SiC/Ti_3SiC_2 interface region and in the fcc-structured Ti_3SiC_2 region. The relative amount of Si in the fcc-structured region increased from ~16 to ~18 at %, whereas Si in the interface region increased from ~35 to ~40 at %. In the fcc-structured Ti_3SiC_2 region, the C atomic % decreases from ~33 to ~30 at % and Ti atomic % remains
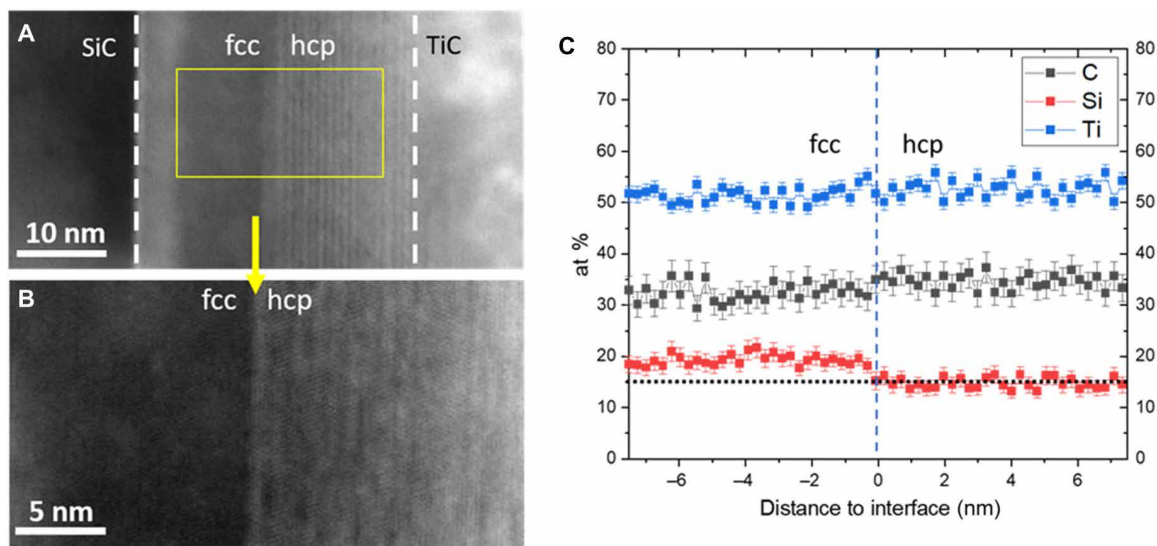

Fig. 3. STEM images and EDS spectra of the SiC substrates and Ti₃SiC₂ films before and after irradiation. (**A**) STEM image of the RT low-dose C irradiated SiC/Ti₃SiC₂/TiC interface region. (**B**) Magnified STEM image of the fcc/hcp Ti₃SiC₂ interface. (**C**) Atomic percent of C, Si, and Ti determined from EDS as a function of distance from the fcc/hcp interface shown in (B). A vertical dashed line is added to mark the position of the interface. A horizontal dashed line corresponds to the C ratio in a stoichiometric Ti₃SiC₂.
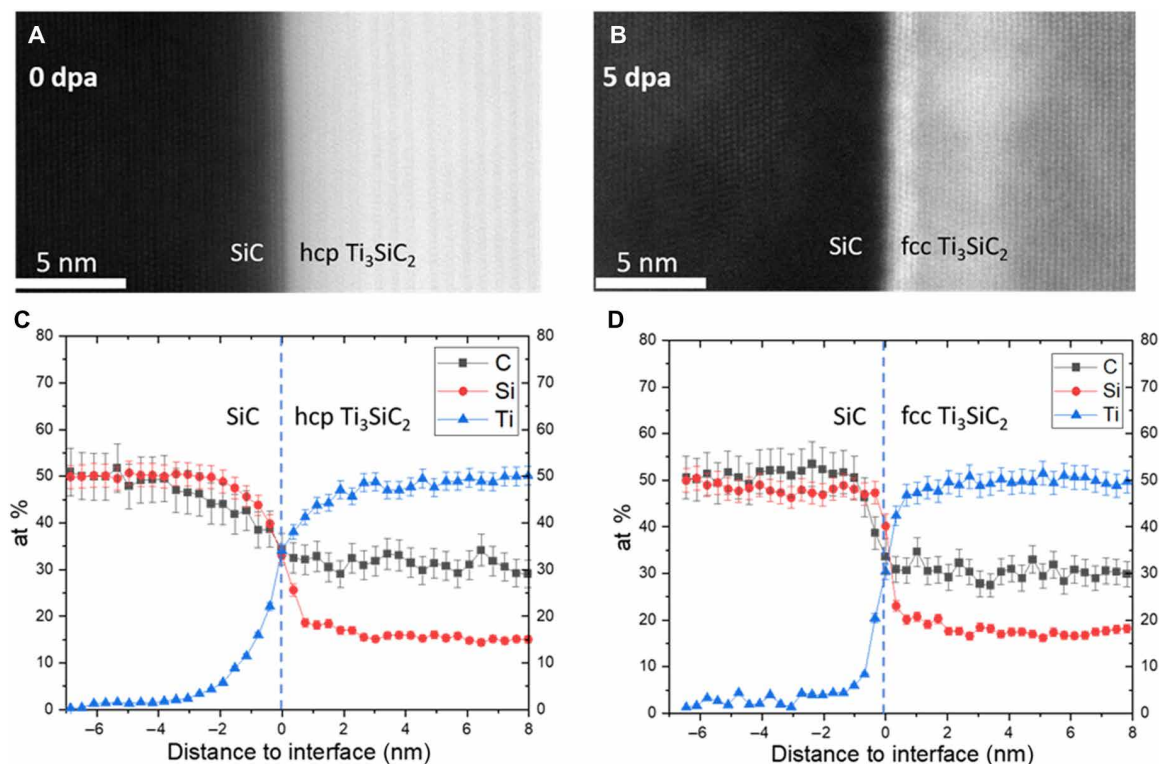
Fig. 4. STEM images and EDS spectra of the SiC substrates and Ti$_3$SiC$_2$ films before and after irradiation at RT, 7.5 × 10^{16} ions·cm$^{−2}$. (**A**) STEM images of SiC/Ti$_3$SiC$_2$ interface region before irradiation and (**B**) after irradiation. Atomic percent of C, Si, and Ti determined from EDS as a function of distance from the fcc/hcp interface (**C**) before irradiation and (**D**) after irradiation. A vertical dashed line is added to mark the position of the interface. The number on the horizontal axis corresponds to the distance to the interface. The average concentration of Si in Ti$_3$SiC$_2$ near the SiC interface has increased from ~16 to ~18 at %, and it decreased in SiC near the Ti$_3$SiC$_2$ interface from ~50 to ~48 at %. The average concentration of Ti and C did not change in an obvious way.

almost unchanged at ~51 at %. This is reasonable when considering the redistribution of Si atoms under irradiation conditions, under which Si atoms in the SiC substrate can be displaced from the sublattice either into the interstitial sites or into the Ti$_3$SiC$_2$ layer region, which could increase the concentration of Si in these regions.

To explain the changes in compositions near the SiC/Ti$_3$SiC$_2$ interface, we have calculated defect formation energies at and near the interface using the density functional theory (DFT) calculations. All the calculated defect energies are given in the Supplementary Materials, and here, we focus on the discussion on defects most relevant to our experimental observations. As shown in Fig. 5A, in the case of SiC, the formation energy of Si interstitials at the interface is much lower than that in the bulk SiC region, suggesting that there is a thermodynamic driving force for Si interstitials to segregate to the interface. The relatively low migration energy barriers of Si interstitials near the interface <0.7 eV within three Si atoms from the interface, the barrier in the bulk region is ~1.26 eV (8) make such radiation-induced segregation of Si interstitials in SiC possible on experimental time scales. This result is consistent with the increase of Si content at the interface region found in our experiments (Fig. 4). At the same time, our DFT calculations show (Fig. 5A) that as Si atoms become displaced by radiation from SiC into Ti$_3$SiC$_2$, either they form interstitials that move into the Si layer regions within Ti$_3$SiC$_2$ and get trapped in Ti$_3$SiC$_2$ or they spontaneously transform into Si$_{Ti}$ antisites via a barrier-less reaction of I$_{Si}$ + Ti$_{Ti}$ ↔ I$_{Ti}$ + Si$_{Ti}$. Meanwhile, we found that once Si$_{Ti}$ is produced, it could be stabilized in Ti$_3$SiC$_2$ due to the high

positive reaction energies for the consuming reactions (e.g., for Si$_{Ti}$ ↔ I$_{Si}$ + V$_{Ti}$, ~2.93 eV and for I$_C$ + Si$_{Ti}$ ↔ C$_{Ti}$ + I$_{Si}$, ~2.34 eV; see table S3.1). Either way, the concentration of Si atoms within the Ti$_3$SiC$_2$ layer would be increased through the displacement of Si atoms from SiC under irradiation. After Ti interstitials have been created through the reaction of I$_{Si}$ + Ti$_{Ti}$ ↔ I$_{Ti}$ + Si$_{Ti}$, they will immediately diffuse into the SiC/Ti$_3$SiC$_2$ interface or the Si layer regions within Ti$_3$SiC$_2$ as shown by arrows in Fig. 5A. This is reasonable when considering that the Ti interstitial in the SiC/Ti$_3$SiC$_2$ region is only stable right at the SiC/Ti$_3$SiC$_2$ interface or the Si layer on the Ti$_3$SiC$_2$ side (see table S1.5). Meanwhile, it is interesting to note that if there is a Si vacancy in the Si layer within Ti$_3$SiC$_2$, Ti interstitials in the Si layer regions will react with the vacancy in a barrierless process to form Ti antisites (I$_{Ti}$ + V$_{Si}$ ↔ Ti$_{Si}$). The capture radius for this reaction is larger than the third nearest neighbor.

In addition to the Si interstitial, our calculations revealed that C interstitials (I$_C$) would also be likely to segregate to the SiC/Ti$_3$SiC$_2$ interface, especially on the Ti$_3$SiC$_2$ side, due to the lower formation energies of I$_C$ at interfaces than that in the bulk region and the relatively low migration energies of I$_C$ (see Fig. 5B). Specifically, the barriers for migration of I$_C$ in the bulk are ~0.88 eV for SiC (8) and ~0.86 eV for Ti$_3$SiC$_2$, suggesting that C atoms would also segregate to the interface.

We have also considered the changes in the chemical composition near the Ti$_3$SiC$_2$/TiC interface. Experimental analysis of this composition is shown in Fig. 6. Before irradiation, the interface is diffuse
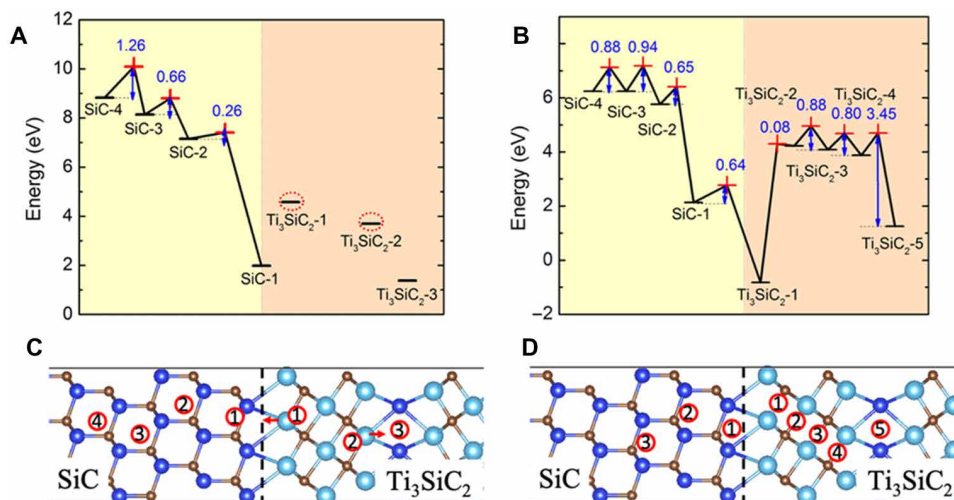
Fig. 5. Formation and migration energies of interstitials near the interface of SiC/Ti₃SiC₂. (**A**) Si interstitials and (**B**) C interstitial near the interface of SiC/Ti₃SiC₂. Horizontal axes in (A) and (B) correspond to positions of interstitials shown in (**C**) and (**D**), respectively. Horizontal black lines on the plot mark formation energies of interstitials, and red crosses represent migration barriers. The red dashed circles in (A) mark Si interstitials that are unstable in that region—these Si interstitials immediately kick a nearby Ti atom out of its sublattice. A complete list of numerical values for the formation and migration energies of Si and C interstitials near the interface of SiC/Ti₃SiC₂ is shown in tables S1.4 and S1.6.
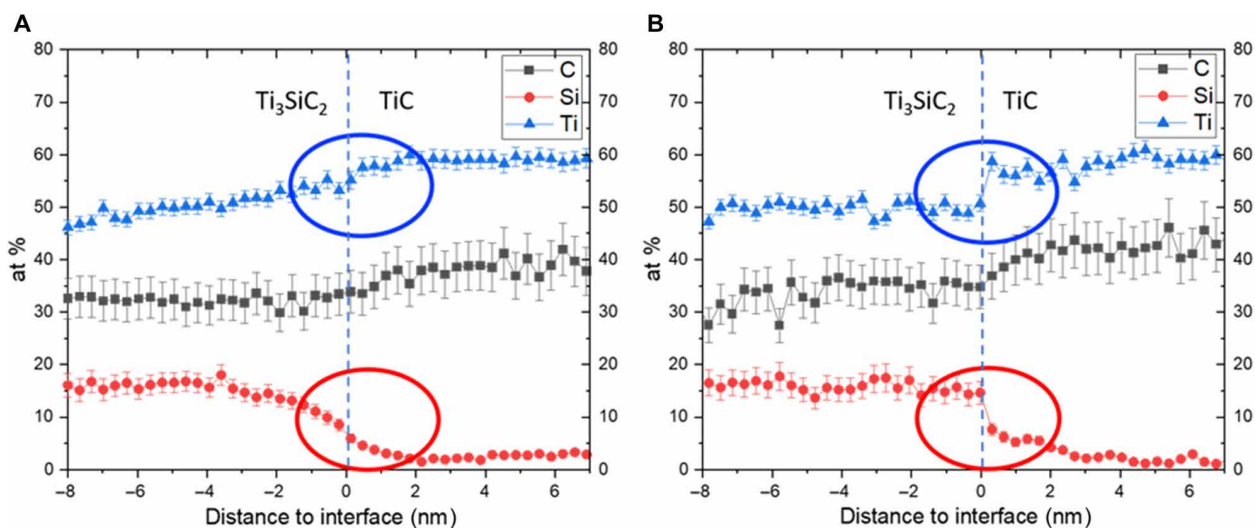

Fig. 6. Atomic percent of C, Si, and Ti determined from STEM-based EDS as a function of distance from the Ti₃SiC₂-TiC interface. (**A**) Before irradiation and (**B**) after irradiation at RT, 7.5×10^{16} ions·cm^{-2}. A vertical dashed line is added to mark the position of the interface. The number in the horizontal axis corresponds to the distance to the interface. The blue and red circles represent the chemical compositions of Ti and Si in the interface regions, respectively. The average concentration of Si has increased in TiC$_x$ near the Ti₃SiC₂ interface from ~2 to ~5 at % after irradiation. The average concentration of Ti and C did not change in an obvious way.

with a thickness of ~5 nm. Ti concentration increases slowly from ~50 at % to ~60 at % between the Ti₃SiC₂ side and the TiC$_x$ side, whereas the Si concentration decreases from ~16 at % to ~0 at % over the same distance. In addition, we find an obvious penetration of Si from Ti₃SiC₂ to TiC before irradiation. This observation can be explained by considering the high concentration of carbon vacancies (V$_C$) in the substochiometric TiC$_x$. These vacancies make it possible to form Si$_C$ antisites in TiC$_x$. The reaction energy for the formation of Si$_C$ (I$_{Si}$ + V$_C$ ↔ Si$_C$) determined from our DFT calculations ranges from −2.47 eV to −4.14 eV on the TiC$_x$ side, suggesting that during the growth of the films, there is a thermodynamic driving force to attract

Si species from Ti₃SiC₂ to TiC$_x$ across the interface. In addition, similarly to the barrierless reaction of I$_{Si}$ + Ti$_{Ti}$ ↔ I$_{Ti}$ + Si$_{Ti}$ in Ti₃SiC₂ near the SiC/Ti₃SiC₂ interface (see discussion of Fig. 5A), Si atoms that originated from Ti₃SiC₂ can spontaneously form antisites Si$_{Ti}$ near the Ti₃SiC₂/TiC interface (around two atomic layers from the interface on both the TiC and Ti₃SiC₂ sides; see table S2.5). The Ti atoms displaced through the above reaction are trapped at the Ti₃SiC₂/TiC interface, and they increase the local Ti concentration.

After irradiation, the change in the composition across the Ti₃SiC₂/TiC interface becomes sharper (the width of the interface is ~1 nm). The change in the distribution of the elements in the interface region

is highly relevant to the defect evolution during irradiation. Under irradiation, Ti lattice atoms and the Si atoms that have been trapped as antisites on the off-stoichiometric TiC_x ($x < 1$) side near the interface (~2 nm from the interface; see Fig. 6A) can be displaced to become interstitials. Although C atoms can be kicked out as well during irradiation, they are expected to quickly recombine with the excess C vacancies that exist in the TiC_x system. The displaced Si and Ti interstitials are expected to form interstitial-V_C complexes in TiC_x. Specifically, previously published DFT calculations (38) have reported that the existence of V_C can significantly reduce the formation energy of Ti interstitials in TiC_x, and have shown that Ti interstitials in TiC_x prefer to exist as a defect complex, involving two V_C and one Ti dumbbell interstitial. According to our DFT calculations, the formation energy for the aforementioned defect complex is ~4.44 eV, which is much lower than the formation energy of the Ti interstitial, ~9.46 eV. In addition, our DFT shows that the migration barrier for this Ti defect complex in bulk TiC_x is ~0.85 eV, which is consistent with the previous DFT calculations performed by Sun *et al.* (38), ~0.93 eV. We found that this migration barrier for Ti defect complex in TiC_x is dramatically reduced to ~0.07 eV at the interface region (approximately within a distance of three atomic layers from the interface). This result suggests that Ti atoms will eventually migrate from the TiC_x side to the interface region, leading to a significant increase in Ti concentration at the interface.

On the other hand, we found that Si atoms, which exist as Si_C antisites on the TiC_x side, become trapped on the TiC_x side of the Ti_3SiC_2/TiC_x interface. Specifically, our DFT calculations show that even in the region close to the interface (around two atomic layers from the interface), the activation energy barrier for the Si atom to move from the C sublattice site to the interface is ~1.41 eV, which means that Si does not diffuse easily to the Ti_3SiC_2/TiC_x interface. As a result, the presence of this interface reduces the concentration of Si interstitials, and hence also of Si_{Ti} in Ti_3SiC_2 (in the presence of Si interstitials, Si_{Ti} can form in Ti_3SiC_2 through the reaction of $I_{Si} + Ti_{Ti} \leftrightarrow I_{Ti} + Si_{Ti}$). As discussed in (39), the formation of Si_{Ti} antisites is a possible reason for radiation-induced phase transformation of Ti_3SiC_2. It is therefore likely that suppression of the formation of Si_{Ti} antisite due to the presence of the TiC_x/Ti_3SiC_2 interface is responsible for the suppression of phase transformation in Ti_3SiC_2 observed in our experiments.

We have also analyzed the chemical compositions in the regions far away from the interfaces to determine if there are any changes in the chemical composition in the bulk-like regions of SiC and TiC. The results from STEM-EDS (Fig. 7) show that there is no obvious change in the average composition before and after irradiation in these bulk regions. The local variation in the composition became larger after irradiation, which can be attributed to the spatial heterogeneity of radiation-induced defects and defect clusters.

DISCUSSION
Our results show that the propensity for radiation-induced phase transformation from the hcp to fcc phase of Ti_3SiC_2 is higher near the SiC/Ti_3SiC_2 interface than near the TiC/Ti_3SiC_2 interface. This trend can be explained by the changes in the chemical composition in the
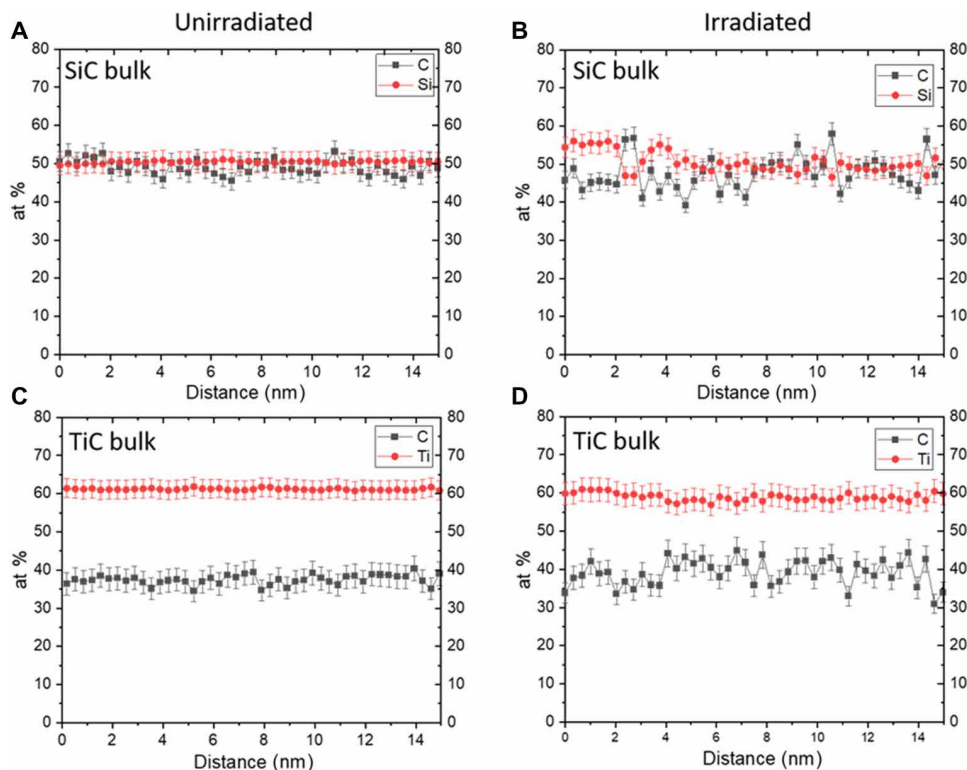

Fig. 7. STEM-based EDS line-scan spectra with a scanned length of 15 nm of SiC and TiC far away from the interface before and after irradiation at RT, 7.5 × 10^{16} ions·cm^{-2}. Unirradiated (**A**) SiC and (**C**) TiC far away from the interface, and irradiated (**B**) SiC and (**D**) TiC far away from the interface.

interface region and in the phase-transformed region. The Si content is higher near the SiC/Ti$_3$SiC$_2$ interface and in the phase-transformed fcc-structured region after irradiation, as compared to the Si content in the hcp-structured Ti$_3$SiC$_2$ region. This trend can be explained by the results of our DFT calculations, which show that it is easier to form Si$_{Ti}$ antisite via the barrierless reaction of I$_{Si}$ + Ti$_{Ti}$ ↔ I$_{Ti}$ + Si$_{Ti}$, in the region close to the SiC/Ti$_3$SiC$_2$ interface. The formation of Si$_{Ti}$ antisite through this reaction in the region close to the TiC/Ti$_3$SiC$_2$ interface is more difficult due to the high concentration of C vacancies in TiC. These C vacancies trap Si atoms at Si$_C$ antisites on the TiC side of the interface.

Our results demonstrate that SiC can act as a source of defects, while TiC$_x$ can act as a sink for defects in the SiC/Ti$_3$SiC$_2$/TiC$_x$ multilayer system. The multilayered ceramics made of Ti$_3$SiC$_2$ and TiC have the potential to improve the radiation resistance of Ti$_3$SiC$_2$ material with respect to the undesirable radiation-induced phase transformation. In contrast, multilayers made of Ti$_3$SiC$_2$ and SiC are likely to accentuate this problem. Our study also shows that the role of interfaces in the design of radiation resistance ceramics is complex, and it is closely tied to the details of defect energy landscape.
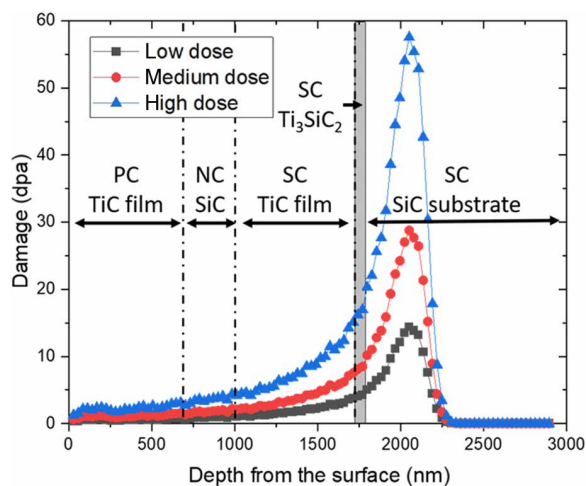

Fig. 8. SRIM calculated damage for 3.15 MeV carbon ion irradiation at 3.0×10^{17} ions·cm^{-2} (high dose), 1.5×10^{17} ions·cm^{-2} (medium dose), and 7.5×10^{16} ions·cm^{-2} (low dose). The gray rectangle represents the single-crystal Ti$_3$SiC$_2$ layer between the single-crystal SiC substrate and the TiC film. PC, polycrystalline; NC, nanocrystalline; SC, single crystal.
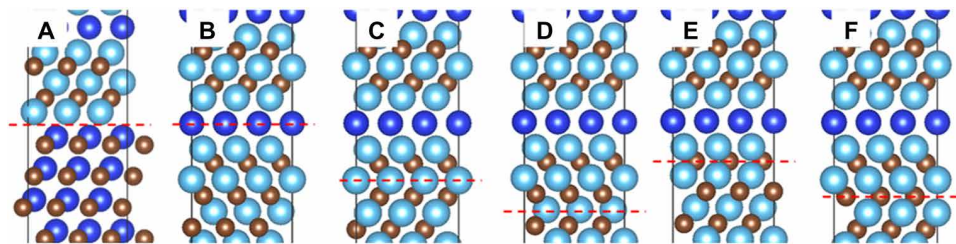
MATERIALS AND METHODS
SiC-Ti$_3$SiC$_2$-TiC multilayer sample preparation
Ti$_3$SiC$_2$ single-crystal films were deposited on 4H-SiC (0001) single-crystal substrates by radio frequency (RF) magnetron sputtering using Ti (99.999% purity), Si (99.999% purity), and C$_2$H$_2$ (99.99% purity) as the source of Ti, Si, and C elements, followed by the deposition of the single-crystal TiC films. The deposition temperature was set to be 800°C by heating the substrate holder. Before the deposition, the specimens were first degreased with a solution of sodium lauryl sulfate and then ultrasonically cleaned with acetone. The samples were then dried, mounted on a copper substrate holder of 120 mm in diameter, and loaded into the magnetron sputtering chamber for deposition. It is well known that there will always be a very thin oxidation layer on the surface of SiC substrates. To remove the oxide layer, a set of samples was pre-etched in the chamber before the deposition of Ti$_3$SiC$_2$. First, the surface of the samples was bombarded with argon ions for 10 min, accelerated by a DC voltage of −200 V, immediately followed by the deposition of the single-crystal Ti$_3$SiC$_2$ film. The thickness of the as-deposited single-crystal Ti$_3$SiC$_2$ film is 30 nm, as evidenced by TEM. TiC film was 700 nm. Another SiC film with a thickness of 300 nm was deposited on the TiC film using Si (99.999% purity) target and C$_2$H$_2$ (99.99% purity) gas at the same temperature. TEM analysis showed that the deposited SiC film was nanocrystalline SiC. A polycrystalline TiC film with a thickness of 700 nm was deposited on the nanocrystalline SiC film at 800°C. High-purity argon (99.99% purity) was used as a sputtering gas at a pressure of 0.10 Pa. RF power was the same for all the experiments and was kept constant at 90 W. Before each deposition, the chamber was pumped to a background pressure of 1×10^{-5} Pa. The negative DC bias applied to the substrate during the deposition process was set at −40 V. The total thickness for the deposited film is 1.7 μm.

Carbon ion irradiation
The carbon ion irradiation was performed using the tandem accelerator in the Ion Beam Laboratory at the University of Wisconsin-Madison with 3.15 MeV carbon ions. The bulk samples were cut into 5 mm by 5 mm by 2 mm for the ion irradiation. The irradiation temperature was kept below 150°C, measured by thermocouples within the heated specimen stage. The typical irradiation flux was kept at ~7.0×10^{11} ions·cm^{-2}·s^{-2}. The irradiation fluence delivered to the samples was 3.0×10^{17} ions·cm^{-2} for the high dose, 1.5×10^{17} ions·cm^{-2} for the medium dose, and 7.5×10^{16} ions·cm^{-2} for the low dose. The total irradiation time is 10 hours for the high-dose irradiation. The background pressure during irradiation was <5×10^{-4} Pa.

Fig. 9. Atomistic models of the SiC/Ti$_3$SiC$_2$ and TiC/Ti$_3$SiC$_2$ interface. (**A**) SiC/Ti$_3$SiC$_2$ interface. (**B** to **F**) Five possible configurations for the TiC/Ti$_3$SiC$_2$ interface. The dark blue spheres are the Si atoms, the light blue spheres are the Ti atoms, and the brown spheres are the C atoms. The red dashed lines are added to mark the positions of the interfaces.

We used the SRIM (40) software to determine the amount of radiation-induced damage as a function of the distance from the SiC free surface. Damage is measured in units of displacements per atom, which describes the number of times that an atom in the target material is displaced for a given fluence. According to Fig. 8, the damage peak for 3.15 MeV C ions in SiC is located at 2.1 μm below the surface. The damage level is relatively flat within the first 1 μm below the surface. The SiC-Ti$_3$SiC$_2$-TiC interface region we studied is located at ~1.7 μm from the surface. The damage in this region is approximately 5, 10, and 20 dpa for the low-, medium-, and high-dose irradiation, respectively.

TEM sample preparation

Samples for the TEM analysis were prepared using a standard lift-out technique by an FEI Helios PFIB G4 focused ion beam (FIB)/field-emission SEM instrument in the Materials Science Center at the University of Wisconsin-Madison. To protect the sample surface from damage during FIB preparation, a 3.0-μm Pt protective layer was deposited on the surface by two steps: (i) A 2 kV electron beam (low energy) was used to deposit a 1.0-μm Pt layer to avoid damage from high-energy ion deposition, and (ii) a 12 kV ion beam was used for the deposition of another 2.0 μm Pt layer. The thinning process was sped up by a high-energy ion beam (30 kV) at the beginning and ended with a low-energy beam (2 kV) to carefully remove the amorphous area generated in the former stage (41).

Experimental TEM and STEM EDS spectrum image data acquisition

FEI Tecnai F30 with field-emission gun TEM was used to analyze the damage and the microstructure before and after irradiation. Detailed structural and chemical analysis of the SiC-Ti$_3$SiC$_2$-TiC film was carried out using high-angle annular dark-field STEM (HAADF-STEM) images and EDS in an FEI Titan G2 80–200 (S)TEM equipped with the Super-X EDS detection system. The microscope was operated at an acceleration voltage of 200 kV, with a probe current of approximately 300 pA and a probe convergence angle of 21 mrad. Simultaneous HAADF and EDS acquisition were performed using the Bruker Esprit software. All the interface and bulk line scans were obtained with a step size of 0.3 nm, a dwell time of 20 s with a spot size of 6 to get a stronger signal, and good statistics. The total scan length was 15 nm. A drift-corrected spectrum was acquired over 100 frames, with a dwell time of 50 μs per pixel and an interval of 30 s between applications of drift correction using the acquired HAADF image. Five different regions for each interface and bulk regions were scanned in different locations to get average results. All five acquisitions used nearby areas of the same sample and approximately the same electron dose. As the counting rate of the EDS signals is also sensitive to the thickness of the samples, the thickness of the samples was measured by electron energy-loss spectroscopy. The results show that the thickness of all the measured regions is around 50 nm.

Computational details

The DFT calculations were performed using the projector augmented-wave (PAW) method (42) and the Perdew-Burke-Ernzerhof for solids (43), as implemented in the Vienna Ab Initio Simulation Package (VASP) (44). The PAW potentials for Ti, Si, and C contained 10, 4, and 4 valence electrons, respectively. The interfacial configuration of SiC/Ti$_3$SiC$_2$ was built consistently with previously published experimental results (45) and is shown in Fig. 9A. The supercell of the SiC/Ti$_3$SiC$_2$ interface was modeled with a slab, in which 15 layers of Ti$_3$SiC$_2$(0001) were stacked on the substrate of eight Si-C bilayers of SiC(111). A 30 Å-thick vacuum layer was added to avoid the interaction between the top and bottom free surface of the slab. In the case of the TiC/Ti$_3$SiC$_2$ interface, it has been commonly reported that the formation of Ti$_3$SiC$_2$ in the TiC matrix is achieved by the incorporation of the Si layer near twin boundaries of TiC (39, 46, 47). Following this strategy, we considered five interfacial configurations with different positions of the Si layer (see Fig. 9, B to F). Similarly to the model of the SiC/Ti$_3$SiC$_2$ interface, the TiC-Ti$_3$SiC$_2$ interfaces were built with at least 16 layers of Ti$_3$SiC$_2$(0001) on the substrate of at least 7 layers of TiC(111) in each slab. A 30-Å-thick vacuum layer was also added to avoid the interaction between the top and bottom surface.

The relative stability of the interfaces can be determined based on the interfacial energy $\gamma = (E_T - \sum_i N_i\mu_i)/A - S_{TiC} - S_{Ti_3SiC_2}$. Here, E_T is the total energy of the supercell and N_i and μ_i are the number of atoms of type i (i = Ti, Si, and C) in the supercell and the corresponding chemical potential, respectively. S_{TiC} and $S_{Ti3SiC2}$ are the surface energies of TiC and Ti$_3$SiC$_2$, respectively. Because the five different supercells have the same numbers of atoms of each type i and the same surface areas, the relative interfacial energy of these interfaces can be determined by comparing the total energies of the supercells. On the basis our DFT calculations, we found that the configuration where the Si layer is located in the interface (i.e., Fig. 9B) has the lowest interfacial energy, and thus, in the following study, we will mainly focus on this configuration.

Within the interface plane, each slab consists of 3 × 3 unit cells. The total numbers of atoms in the SiC/Ti$_3$SiC$_2$ and TiC/Ti$_3$SiC$_2$ slabs are 279 and 243, respectively. To form coherent interfaces, in-plane lattice constants of Ti$_3$SiC$_2$ (c/a = 5.772, a = 3.075 Å) were expanded by 0.68% and −0.26% to match those of the stiffer SiC (3.096 Å) and TiC (3.067 Å), respectively. Because of the small lattice-constant mismatch, as a first approximation, we neglected the effect of potential misfit dislocations. All calculations were performed with the energy cutoff of 520 eV for the plane-wave basis set. A 3 × 3 × 1 k-point mesh was used for integrations over the Brillouin zone. Errors from both the cutoff energy and the k-point convergence were smaller than 1 meV per atom. The supercells were fully relaxed (i.e., we relaxed the atomic coordinates) until the forces on the ions converged to below 1×10^{-2} eV/Å.

The formation energies of defects were calculated as follows

$$E_f(\text{def}) = E_T(\text{def}) - E_T + \sum_i n_i\mu_i$$

where $E_T(\text{def})$ is the total energy of a supercell with one defect, n_i is the number of atoms of type i removed from the system ($n_i > 0$) to form vacancies, and μ_i is the chemical potential of atom i. In the multilayer samples, all these SiC, TiC, and Ti$_3$SiC$_2$ crystals coexist, and in this case, the chemical potentials of Si, C, and Ti were determined from the following relations: $\mu_{SiC} = \mu_{Si} + \mu_C$, $\mu_{TiC} = \mu_{Ti} + \mu_C$, and $\mu_{Ti3SiC2} = 3\mu_{Ti} + \mu_{Si} + 2\mu_C$. We have taken $\mu_{Si} = -5.68$ eV, $\mu_{Ti} = -9.36$ eV, and $\mu_C = -9.39$ eV, following (11, 48). Last, the diffusion pathways and migration energy barriers for defects were determined by the climbing-image nudged elastic band (CI-NEB) method (49) (typically with five images).

SUPPLEMENTARY MATERIALS

REFERENCES AND NOTES

1. O. Wilhelmsson, P. Eklund, F. Giuliani, H. Högberg, L. Hultman, U. Jansson, Intrusion-type deformation in epitaxial Ti$_3$SiC$_2$/Ti C$_{0.67}$ nanolaminates. *Appl. Phys. Lett.* **91**, 123124 (2007).
2. C. E. Athanasiou, H. Zhang, C. Ramirez, J. Xi, T. Baba, X. Wang, W. Zhang, N. P. Padture, I. Szlufarska, B. W. Sheldon, High toughness carbon-nanotube-reinforced ceramics *via* ion-beam engineering of interfaces. *Carbon* **163**, 169–177 (2020).
3. R. Porat, Experimental study multilayer cvd coatings of Tic+ Tin and their effect on cutting tool life. *Surf. Eng.* **8**, 292–294 (1992).
4. H. Holleck, V. Schier, Multilayer PVD coatings for wear protection. *Surf. Coat. Technol.* **76–77**, 328–336 (1995).
5. Y. Cai, L. Cheng, X. Yin, H. Yin, N. Wang, H. Zhang, Y. Wang, Effect of positioning impregnation on the oxidation behaviour of Ti$_3$SiC$_2$/SiC functionally graded materials at 1400 °C. *J. Alloys Compd.* **742**, 180–190 (2018).
6. C. Liu, J. Xi, I. Szlufarska, Sensitivity of SiC grain boundaries to oxidation. *J. Phys. Chem. C* **123**, 11546–11554 (2019).
7. X. Wang, H. Zhang, T. Baba, H. Jiang, C. Liu, Y. Guan, O. Elleuch, T. Kuech, D. Morgan, J. C. Idrobo, P. M. Voyles, I. Szlufarska, Radiation-induced segregation in a ceramic. *Nat. Mater.* **19**, 992–998 (2020).
8. H. Gleiter, Grain boundaries as point defect sources or sinks––Diffusional creep. *Acta Metall.* **27**, 187–192 (1979).
9. G. S. Was, J. P. Wharry, B. Frisbie, B. D. Wirth, D. Morgan, J. D. Tucker, T. R. Allen, Assessment of radiation-induced segregation mechanisms in austenitic and ferritic-martensitic alloys. *J. Nucl. Mater.* **411**, 41–50 (2011).
10. J. Xi, B. Liu, F. Yuan, Y. Zhang, W. J. Weber, Diffusion of point defects near stacking faults in 3C-SiC via first-principles calculations. *Scr. Mater.* **139**, 1–4 (2017).
11. J. Xi, B. Liu, Y. Zhang, W. J. Weber, Ab initio study of point defects near stacking faults in 3C-SiC. *Comput. Mater. Sci.* **123**, 131–138 (2016).
12. M. Ames, J. Markmann, R. Karos, A. Michels, A. Tschöpe, R. Birringer, Unraveling the nature of room temperature grain growth in nanocrystalline materials. *Acta Mater.* **56**, 4255–4266 (2008).
13. T. Chookajorn, H. A. Murdoch, C. A. Schuh, Design of stable nanocrystalline alloys. *Science* **337**, 951–954 (2012).
14. W. Han, M. J. Demkowicz, N. A. Mara, E. Fu, S. Sinha, A. D. Rollett, Y. Wang, J. S. Carpenter, I. J. Beyerlein, A. Misra, Design of radiation tolerant materials via interface engineering. *Adv. Mater.* **25**, 6975–6979 (2013).
15. M. Ishimaru, Y. Zhang, S. Shannon, W. J. Weber, Origin of radiation tolerance in 3C-SiC with nanolayered planar defects. *Appl. Phys. Lett.* **103**, 033104 (2013).
16. Y. Zhang, M. Ishimaru, T. Varga, T. Oda, C. Hardiman, H. Xue, Y. Katoh, S. Shannon, W. J. Weber, Nanoscale engineering of radiation tolerant silicon carbide. *Phys. Chem. Chem. Phys.* **14**, 13429–13436 (2012).
17. L. Jamison, M.-J. Zheng, S. Shannon, T. Allen, D. Morgan, I. Szlufarska, Experimental and ab initio study of enhanced resistance to amorphization of nanocrystalline silicon carbide under electron irradiation. *J. Nucl. Mater.* **445**, 181–189 (2014).
18. C. Schubert, U. Kaiser, A. Hedler, W. Wesch, T. Gorelik, U. Glatzel, J. Kräußlich, B. Wunderlich, G. Heß, K. Goetz, Nanocrystal formation in SiC by Ge ion implantation and subsequent thermal annealing. *J. Appl. Phys.* **91**, 1520–1524 (2002).
19. L. Jamison, K. Sridharan, S. Shannon, I. Szlufarska, Temperature and irradiation species dependence of radiation response of nanocrystalline silicon carbide. *J. Mater. Res.* **29**, 2871–2880 (2014).
20. X. Zhang, E. G. Fu, A. Misra, M. J. Demkowicz, Interface-enabled defect reduction in He ion irradiated metallic multilayers. *JOM* **62**, 75–78 (2010).
21. D. J. Tallman, L. He, J. Gan, E. N. Caspi, E. N. Hoffman, M. W. Barsoum, Effects of neutron irradiation of Ti$_3$SiC$_2$ and Ti$_3$AlC$_2$ in the 121–1085 °C temperature range. *J. Nucl. Mater.* **484**, 120–134 (2017).
22. R. Su, H. Zhang, D. J. O'Connor, L. Shi, X. Meng, H. Zhang, Deposition and characterization of Ti$_2$AlC MAX phase and Ti$_3$AlC thin films by magnetron sputtering. *Mater. Lett.* **179**, 194–197 (2016).
23. R. Su, H. Zhang, X. Meng, L. Shi, C. Liu, Synthesis of Cr$_2$AlC thin films by reactive magnetron sputtering. *Fusion Eng. Des.* **125**, 562–566 (2017).
24. X. Lu, S. Li, W. Zhang, W. Yu, Y. Zhou, Thermal shock behavior of a nanolaminated ternary boride: MoAlB. *Ceram. Int.* **45**, 9386–9389 (2019).
25. J.-F. Li, W. Pan, F. Sato, R. Watanabe, Mechanical properties of polycrystalline Ti$_3$SiC$_2$ at ambient and elevated temperatures. *Acta Mater.* **49**, 937–945 (2001).
26. T. El-Raghy, M. W. Barsoum, Diffusion kinetics of the carburization and silicidation of Ti$_3$SiC$_2$. *J. Appl. Phys.* **83**, 112–119 (1998).
27. N. G. Jones, C. Humphrey, L. D. Connor, O. Wilhelmsson, L. Hultman, H. J. Stone, F. Giuliani, W. J. Clegg, On the relevance of kinking to reversible hysteresis in MAX phases. *Acta Mater.* **69**, 149–161 (2014).
28. R. Gadiou, S. Serverin, P. Gibot, C. Vix-Guterl, The synthesis of SiC and TiC protective coatings for carbon fibers by the reactive replica process. *J. Eur. Ceram. Soc.* **28**, 2265–2274 (2008).
29. S. J. Zinkle, J. T. Busby, Structural materials for fission & fusion energy. *Mater. Today* **12**, 12–19 (2009).
30. C. Furgeaud, F. Brenet, J. Nicolai, Multiscale study of Ti$_3$SiC$_2$ thin film growth mechanisms obtained by magnetron sputtering. *Materialia* **7**, 100369 (2019).
31. R. Su, H. Zhang, L. Shi, H. Wen, Formation of nanostructures in Ti$_2$AlC induced by high-temperature helium irradiation. *J. Eur. Ceram. Soc.* **39**, 1993–2002 (2019).
32. T. Yang, C. Wang, W. Liu, S. Liu, J. Xiao, Q. Huang, J. Xue, S. Yan, Y. Wang, Formation of nano-twinned structure in Ti$_3$AlC$_2$ induced by ion-irradiation. *Acta Mater.* **128**, 1–11 (2017).
33. W. S. Williams, Physics of transition metal carbides. *Mater. Sci. Eng.* **105–106**, 1–10 (1988).
34. H. Zhang, R. Su, L. Shi, D. J. O'Connor, H. Wen, Structural changes of Ti$_3$SiC$_2$ induced by helium irradiation with different doses. *Appl. Surf. Sci.* **434**, 1210–1216 (2018).
35. C. Wang, T. Yang, C. L. Tracy, C. Lu, H. Zhang, Y. J. Hu, L. Wang, L. Qi, L. Gu, Q. Huang, J. Zhang, J. Wang, J. Xue, R. C. Ewing, Y. Wang, Disorder in M$_{n+1}$AX$_n$ phases at the atomic scale. *Nat. Commun.* **10**, 622 (2019).
36. H. Zhang, R. Su, L. Shi, D. J. O'Connor, B. V. King, E. H. Kisi, The damage evolution of He irradiation on Ti$_3$SiC$_2$ as a function of annealing temperature. *J. Eur. Ceram. Soc.* **38**, 1253–1264 (2018).
37. W. A. Hanson, M. K. Patel, M. L. Crespillo, F. Zhang, S. J. Zinkle, Y. Zhang, W. J. Weber, Ionizing vs collisional radiation damage in materials: Separated, competing, and synergistic effects in Ti$_3$SiC$_2$. *Acta Mater.* **173**, 195–205 (2019).
38. W. Sun, H. Ehteshami, P. R. C. Kent, P. A. Korzhavyi, Self-diffusion of Ti interstitial based point defects and complexes in TiC. *Acta Mater.* **165**, 381–387 (2019).
39. R. Yu, L. L. He, H. Q. Ye, Effects of Si and Al on twin boundary energy of TiC. *Acta Mater.* **51**, 2477–2484 (2003).
40. J. F. Ziegler, M. D. Ziegler, J. P. Biersack, SRIM—The stopping and range of ions in matter (2010). *Nucl. Instrum. Methods Phys. Res. Sect. B Beam Interact. Mater. Atoms* **268**, 1818–1823 (2010).
41. H. Luo, H. Sheng, H. Zhang, F. Wang, J. Fan, J. Du, P. Ping Liu, I. Szlufarska, Plasticity without dislocations in a polycrystalline intermetallic. *Nat. Commun.* **10**, 3587 (2019).
42. G. Kresse, J. Furthmüller, Efficient iterative schemes for ab initio total-energy calculations using a plane-wave basis set. *Phys. Rev. B* **54**, 11169–11186 (1996).
43. G. Kresse, D. Joubert, From ultrasoft pseudopotentials to the projector augmented-wave method. *Phys. Rev. B* **59**, 1758–1775 (1999).
44. J. P. Perdew, K. Burke, M. Ernzerhof, Generalized gradient approximation made simple. *Phys. Rev. Lett.* **77**, 3865–3868 (1996).
45. Z. Wang, S. Tsukimoto, M. Saito, K. Ito, M. Murakami, Y. Ikuhara, Ohmic contacts on silicon carbide: The first monolayer and its electronic effect. *Phys. Rev. B* **80**, 245303 (2009).
46. R. Yu, Q. Zhan, L. L. He, Y. C. Zhou, H. Q. Ye, Si-induced twinning of TiC and formation of Ti$_3$SiC$_2$ platelets. *Acta Mater.* **50**, 4127–4135 (2002).
47. M. W. Barsoum, Comment on "Reaction layers around SiC particles in Ti: An electron microscopy study". *Scr. Mater.* **43**, 285–286 (2000).
48. J. Xi, H. Jiang, C. Liu, D. Morgan, I. Szlufarska, Corrosion of Si, C, and SiC in molten salt. *Corros. Sci.* **146**, 1–9 (2019).
49. G. Henkelman, B. P. Uberuaga, H. Jónsson, A climbing-image nudged elastic band method for finding saddle points and minimum energy paths. *J. Chem. Phys.* **113**, 9901 (2000).
50. Y.-R. Lin, C.-Y. Ho, W.-T. Chuang, C.-S. Ku, J.-J. Kai, Swelling of ion-irradiated 3C-SiC characterized by synchrotron radiation based XRD and TEM. *J. Nucl. Mater.* **455**, 292–296 (2014).
51. S. Agarwal, T. Koyanagi, A. Bhattacharya, L. Wang, Y. Katoh, X. Hu, M. Pagan, S. J. Zinkle, Neutron irradiation-induced microstructure damage in ultra-high temperature ceramic TiC. *Acta Mater.* **186**, 1–10 (2020).
52. B. Tyburska-Püschel, Y. Zhai, L. He, C. Liu, A. Boulle, P. M. Voyles, I. Szlufarska, K. Sridharan, Size distribution of black spot defects and their contribution to swelling in irradiated SiC. *J. Nucl. Mater.* **476**, 132–139 (2016).